Modeling the Effects of Positive and Negative Feedback in Kidney Blood Flow Control

Runjing Liu
Mentor: Dr. Anita Layton

A thesis submitted to the Department of Mathematics for honors

Duke University, Durham, NC

April 2016

Abstract

This paper models the interactions of three key feedback mechanisms that regulate blood flow in the mammalian kidney: **1.** the myogenic response, triggered by blood pressure in the afferent arteriole; **2.** tubuloglomerular feedback (TGF), a *negative* feedback mechanism responding to chloride concentrations at the mascula densa (MD); and **3.** connecting tubule glomerular feedback (CTGF), a *positive* feedback mechanism responding to chloride concentrations in the connecting tubule, downstream of the mascula densa. Previous models have studied the myogenic response and TGF. However, CTGF is much less well understood, and we thus aim to construct a mathematical model incorporating all three mechanisms. A bifurcation analysis was performed on this expanded model to predict the behavior of the system over a range of physiologically realistic parameters, and numerical simulations of the model equations were computed to supplement the results of the bifurcation analysis. In doing so, we seek to elucidate the interactions of all three feedback mechanisms and their effects on kidney blood flow. In particular, numerical simulations were able to confirm our hypothesis that the interactions between TGF and CTGF give rise to an experimentally observed low frequency oscillation that could not be explained by previous models incorporating TGF alone.

1. Introduction

The kidney performs the essential physiological functions of regulating the balance of water, salt, and blood pressure by filtering, reabsorbing, and secreting controlled amounts of solute and water. The functional unit of the kidney is the nephron which consists of the glomerulus, composed of a bundle of capillaries, and the renal tubule, lined by a single layer of epithelial cells that mediate solute absorption/reabsorption across tubule walls (Eaton and Pooler, 2013). The rat kidney contains ∼40,000 nephrons (Pennell et al., 1974) while the human kidney contains ∼1 million.

Blood is delivered by the afferent arteriole to the glomerulus, where it is filtered so that only fluid and smaller solutes enter the nephron, while larger blood cells and proteins are kept in the bloodstream. The single nephron glomerular filtration rate (SNGFR) is controlled by the muscle tone of the afferent arteriole; SNGFR decreases in response to vasoconstriction, while SNGFR increases in response to vasodilation. One important feedback regulator of SNGFR is the myogenic response, where vasoconstriction occurs after an increase in afferent arteriole blood pressure.

The filtrate, having now entered the nephron, begins the process of being transformed into urine. Our model will be focused upon the portions of the nephron known as the thick ascending limb (TAL) and the distal tubule (DT). The TAL is a water impermeable section of the nephron where chloride ions are reabsorbed from the filtrate back into the body. At the end of the TAL is a collection of cells known as the mascula densa (MD), which detects chloride concentration and generates regulatory signals in a negative feedback loop (see Fig. 1 for a schematic of the nephron). For example, should chloride concentration at the MD be too high, signals are sent to constrict the afferent arteriole, which in turn lowers SNGFR. The lower tubular flow results in a longer transit time through the TAL, which allows for more chloride to be absorbed and concentration to be lowered. The opposite occurs should the concentration at MD be too low. This negative feedback loop is known as tubuloglomerular feedback (TGF) (Layton and Edwards, 2014).

In a previous model, TGF has been shown to generate limit cycle behavior in variables such as SNGFR, fluid flow through the TAL, concentration at MD, and diameter of the afferent arteriole (Ford Versypt et al., 2015). In these oscillations generated by TGF, we observe only one dominant frequency

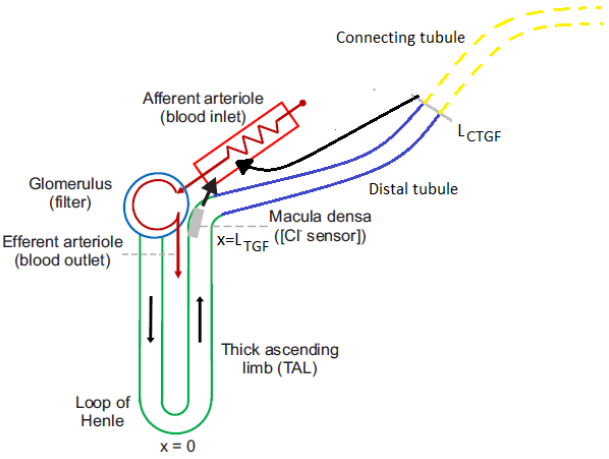

Figure 1: A schematic of the nephron, adapted from Versypt et al (2015).

of ∼25-40 mHz. Yet experimentally, a second slower mode of oscillation of less than 10mHz can also be observed, which cannot be explained by TGF alone (Fig. 2).

Therefore, this project seeks to explain the appearance of this slower mode of oscillation. One potential cause may be the less-understood connecting tubule glomerular feedback (CTGF): experimental evidence has shown that increased chloride concentration in the connecting tubule dilates the afferent arteriole, resulting in a *positive* feedback loop (Ren et al., 2007, 2010). The precise functional roles CTGF remain controversial.

However, we hypothesize that such a positive feedback mechanism may explain the slower mode of oscillation. We remark that the fundamental frequency of a limit cycle oscillation is dictated by the time delay of the feedback. In limit cycles generated by TGF, the delay is the transit time of a fluid packet to travel from the glomerulus to the MD and trigger a signal plus the time it takes this signal from the MD to affect the afferent arteriole. In CTGF, the delay is longer since the fluid packet must travel past the MD and through the distal tubule to reach the downstream connecting tubule and trigger a signal. Hence, if one envisions CTGF as a limit cycle generator, then we would expect such CTGF limit cycles to have a fundamental frequency lower than that of TGF. However, because CTGF is a positive feedback loop, it cannot generate oscillations by itself. But because both TGF and CTGF affect the afferent arteriole, CTGF signals can be viewed as periodic

perturbations to TGF mediated limit cycles; hence, there is potential to obtain oscillations of two overlapping frequencies: one corresponding to the TGF fundamental frequency of 25-40 mHz and another corresponding to the lower CTGF frequency.

To investigate, we expanded the earlier model (Arciero et al., 2015) to include the distal tubule and positive feedback. A bifurcation analysis was done on this new model to examine the effects of key parameters such as feedback loop sensitivity or feedback delay. Furthermore, we compare our bifurcation analysis against direct numerical simulations, and such simulations suggest that the interactions of TGF and CTGF do in fact produce the desired slow oscillation, but the slow oscillation appears to be transient.

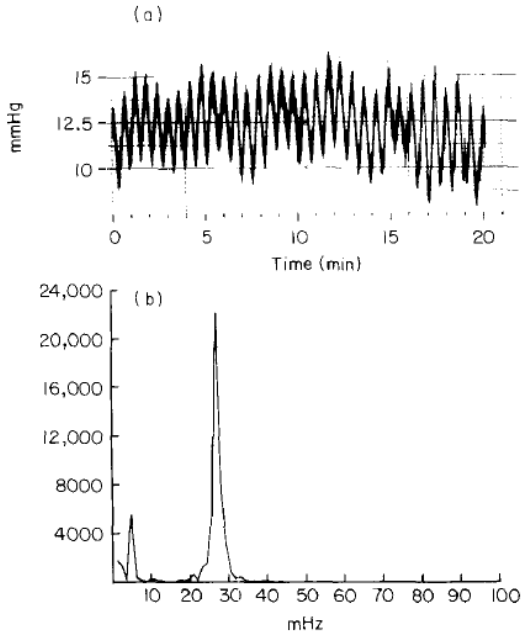

Figure 2: Experimental pressure record from proximal tubule of Wistar-Kyoto (WKY) rat showing a spontaneous limit-cycle oscillation (panel a) and the power spectrum for that limit cycle oscillation, in arbitrary units, showing relative strength of frequency components (panel b). Figure adapted from (Holstein-Rathlou and Leyssac, 1986) with permission.

2. Model Equations

We have extended a previous model of TGF and solute transport along the thick ascending limb (Arciero et al., 2015; Ford Versypt et al., 2015) to include the distal tubule and CTGF. Below we describe the system of equations used to model fluid and solute transport along the nephron segments. $C(x,t)$ is the tubule fluid chloride concentration at time t and position x (see Fig. 1). The partial differential equation (PDE) describing $C(x,t)$ (Eq. 1-2) is coupled to a system of ordinary differential equations (ODEs) governing the diameter $D(t)$ and the smooth muscle activation $A(t)$ of the afferent arteriole (Eq. 3 and 4 respectively).

$$\pi r^2 \frac{\partial}{\partial t} C(x,t) = -\frac{\partial}{\partial x}[F_{\mathrm{TAL}}(D(t))C(x,t)] - 2\pi r\left(\frac{V_{max,TAL}C(x,t)}{K_{m,TAL}+C(x,t)} + p(C(x,t)-C_e(x))\right), \quad 0 \le x \le L_{\mathrm{TGF}} \tag{1}$$

$$\pi r^2 \frac{\partial}{\partial t} C(x,t) = -\frac{\partial}{\partial x}[F_{\mathrm{DT}}(D(t),x)C(x,t)] - 2\pi r\left(\frac{V_{max,DT}C(x,t)}{K_{m,DT}+C(x,t)}\right), \quad L_{\mathrm{TGF}} < x \le L_{\mathrm{CTGF}} \tag{2}$$

$$\frac{d}{dt}D(t) = \frac{1}{t_d}\frac{2}{P_{avg,c}}\left(\frac{P_{avg}D(t)}{2} - T_{total}(D(t),A(t))\right) \tag{3}$$

$$\frac{d}{dt}A(t) = \frac{1}{t_a}\left(A_{total}(C(L_{\mathrm{TGF}},t-\tau_{\mathrm{TGF}}),C(L_{\mathrm{CTGF}},t-\tau_{\mathrm{CTGF}}),D(t)) - A(t)\right) \tag{4}$$

Note that the PDE for $C(x,t)$ is defined in a piecewise manner: $0 \le x \le L_{\mathrm{TGF}}$ corresponds to the TAL, whereas $L_{\mathrm{TGF}} < x \le L_{\mathrm{CTGF}}$ corresponds to the distal tubule. Along both segments (Eq. 1 and Eq. 2), the first term on the right-hand-side represents advective Cl^- transport through the tubule; the second term describes the reabsorption of Cl^- from the tubule using Michaelis-Menten kinetics. We also added an additional term in the TAL piece (Eq. 1) to describe diffusion of Cl^- across the tubule wall with permeability p and extratubular chloride concentration $C_e(x)$ given by:

$$C_e(x) = C_0(Be^{-2x/L_{\mathrm{TGF}}} + (1-B)), \qquad 0 \le x \le L_{\mathrm{TGF}} \tag{5}$$

where B is

$$B = (1 - C_{e,\mathrm{MD}}/C_0)/(1 - e^{-2}) \tag{6}$$

We assume that the intra- and extratubular chloride ion concentrations at the bend of the loop of Henle are taken to be: $C_0 = C(0,t) = 275\mathrm{mM}$.

We remark that since the TAL is water impermeable, its tubular flow F_{TAL} is constant in space and depends only on the afferent arteriole diameter $D(t)$. In contrast, the distal tubule is water permeable, so F_{DT} not only depends on $D(t)$ but varies in space as well. We assume that water absorption is constant through the distal tubule, and therefore F_{DT} decreases linearly. The equations for flows F_{TAL} and F_{DT} are:

$$F_{\mathrm{TAL}}(D(t)) = \alpha Q_A = \alpha \frac{\pi D(t)^4 \Delta P}{128 \mu l} \tag{7}$$

$$F_{\mathrm{DT}}(D(t), x) = F_{\mathrm{TAL}}(D(t)) - \frac{x - L_{\mathrm{TGF}}}{L_{\mathrm{CTGF}} - L_{\mathrm{TGF}}} J F_{\mathrm{TAL}}(D(t)) \tag{8}$$

Q_A is the afferent arteriole flow rate, which follows Poiseuille's Law and depends on: diameter $D(t)$; the pressure drop along the afferent arteriole ΔP; viscosity μ; and afferent arteriole segment length l. α is the fraction of the afferent arteriole flow that enters the TAL. J in Eq. 8 is the fraction of water absorbed by the end of the distal tubule.

In Eq. 3, T_{total} is the tension in the afferent arteriole wall, and is a sum of passive and active components (T_{pass} and T_{act}^{max} respectively):

$$T_{total}(D(t), A(t)) = T_{pass}(D(t)) + A(t) T_{act}^{max}(D(t)) \tag{9}$$

$$T_{pass}(D(t)) = c_{pass} \exp\big(c_{pass,1}(D(t)/D_0 - 1)\big) \tag{10}$$

$$T_{act}^{max}(D(t)) = c_{act} \exp\left[- \left(\frac{D(t)/D_0 - c_{act,1}}{c_{act,2}} \right)^2 \right] \tag{11}$$

Finally, Eq. 4 describes the overall feedback response of the afferent arteriole, driven by variations in $[\mathrm{Cl}^-]$ at the mascula densa (the TGF response) and at the distal tubule exit (the CTGF response), with feedback delays τ_{TGF} and τ_{CTGF} respectively. In previous studies, only TGF is considered. Here we expand the response to include positive feedback from the distal tubule.

To achieve that goal, we reformulate the target activation A_{total} as:

$$A_{total} = \frac{1}{1 + \exp\Big[- S_{tone}\Big(C(L_{\mathrm{TGF}}, t - \tau_{\mathrm{TGF}}), C(L_{\mathrm{CTGF}}, t - \tau_{\mathrm{CTGF}}), D(t) \Big)\Big]} \tag{12}$$

where S_{tone} is given by

$$\begin{aligned} S_{tone} =& c_{myo} \frac{P_{avg} D(t)}{2} + \frac{c_2}{1 + \exp[-c_{\mathrm{TGF}}(C(L_{\mathrm{TGF}}, t - \tau_{\mathrm{TGF}}) - C_{\mathrm{TGF,op}})]} \\ & - \frac{c_3}{1 + \exp[-c_{\mathrm{CTGF}}(C(L_{\mathrm{CTGF}}, t - \tau_{\mathrm{CTGF}}) - C_{\mathrm{CTGF,op}})]} - c_{tone} \end{aligned} \tag{13}$$

Parameter values are summarized in Table 1, and justification of key parameters concerning TGF and myogenic response can be found in previous studies (Arciero et al., 2015; Ford Versypt et al., 2015). However, the new CTGF parameters are not well characterized, so we assume c_{CTGF} to be equal to c_{TGF} and let c_3 take on a value similar to c_2 such that the model predicts oscillations in the base case.

3. Results

3.1. The characteristic equations

We aim to better understand the model's long term dynamics over the range of physiologically relevant parameter values. One way to accomplish this is to solve numerical solutions for the model equations (Eq. 1–4). However, because the model involves many parameters, it is not feasible to perform numerical simulations for every combination of parameter values. Moreover, we are typically interested in asymptotic behavior and such long-time computation of coupled PDEs is relatively time intensive. Instead, we first perform a bifurcation analysis and begin by deriving the characteristic equa-

tion. In general, we have the model equations (Eq. 1–4) to be of the form:

$$\frac{\partial}{\partial t}C_1(x,t) = F^{(0)}(D(t))\frac{\partial}{\partial x}C_1(x,t) + F^{(1)}(C_1(x,t)) \quad 0 \le x \le L_{\text{TGF}} \tag{14}$$

$$\frac{\partial}{\partial t}C_2(x,t) = \frac{\partial}{\partial x}[F^{(a)}(D(t),x)C_2(x,t)] + F^{(b)}(C_2(x,t)) \quad 0 \le x \le L_{\text{DT}} \tag{15}$$

$$\frac{d}{dt}D(t) = F^{(2)}(D(t),A(t)) \tag{16}$$

$$\frac{d}{dt}A(t) = F^{(3)}(D(t),A(t),C_1(L_{\text{TGF}},t-\tau_{\text{TGF}}),C_2(L_{\text{CTGF}},t-\tau_{\text{CTGF}})) \tag{17}$$

We have split the piecewise equations (Eqs. 1–2) into two variables C_1 and C_2 in order to simplify the algebraic manipulation. However, they still remain coupled as we require that $C_1(L_{\text{TGF}},t) = C_2(0,t)$ to ensure continuity between the TAL and the distal tubule. By comparing Eqs. 1–4 and Eqs. 14–17, one sees the following correspondence: $F^{(0)}$ and $F^{(a)}$ are the advective transport equations; $F^{(1)}$ and $F^{(b)}$ denote the Cl^- reabsorption equations; $F^{(2)}$ is the equation modeling afferent arteriole diameter; and $F^{(3)}$ represents afferent arteriole muscle activation. L_{DT} is defined as $L_{\text{CTGF}} - L_{\text{TGF}}$, the length of the distal tubule. We then linearize these equations about a steady state (denote the steady state values $\bar{D}, \bar{A}, \bar{C_1}(x), \bar{C_2}(x)$), and assume a solution of the form

$$\begin{pmatrix} C_1(x,t) \\ C_2(x,t) \\ D(t) \\ A(t) \end{pmatrix} = \begin{pmatrix} \overline{C}_1(x) \\ \overline{C}_2(x) \\ \overline{D} \\ \overline{A} \end{pmatrix} + \begin{pmatrix} f_1(x) \\ f_2(x) \\ b_1 \\ b_2 \end{pmatrix} e^{\lambda t} \tag{18}$$

And again in accordance with our coupling of C_1 and C_2, we require that $f_2(0) = f_1(L_{\text{TGF}})$. We also fix $f_1(0) = 0$ so that $C_1(0,t) = \overline{C}_1(0)$. Then after algebraic manipulations (see appendix) we arrive at a characteristic equation that relates λ to all the other parameters:

$$\begin{aligned} 1 = &-(K_1+K_2)\left(\frac{F_D^{(0)}(\bar{D})}{F^{(0)}(\bar{D})}\right)\int_0^{L_{\text{TGF}}} \bar{C_1}(z)e^{\lambda(L_{\text{TGF}}-z)/F^{(0)}(\bar{D})}\exp\left(-\int_z^{L_{\text{TGF}}}\left(\frac{F_{C_1}^{(1)}(\bar{C_1}(y))}{F^{(0)}(\bar{D})}\right)dy\right)dz \\ &- K_2\int_0^{L_{\text{DT}}}\left(\frac{\frac{\partial}{\partial z}(F_D^{(a)}(\bar{D},z)\bar{C_2}(z))}{F^{(a)}(\bar{D},z)}\right)\exp\left(\int_z^{L_{\text{DT}}}\left(\frac{\lambda - \frac{\partial}{\partial y}F^{(a)}(\bar{D},y) - F_{C_2}^{(b)}(\bar{C_2}(y))}{F^{(a)}(\bar{D},y)}\right)dy\right)dz \end{aligned} \tag{19}$$

where K_1 and K_2 are

$$K_1 = \frac{F_A^{(2)} F_{C_1}^{(3)} e^{-\lambda \tau_{\mathrm{TGF}}}}{(\lambda - F_A^{(3)})(\lambda - F_D^{(2)}) - F_A^{(2)} F_D^{(3)}} \tag{20}$$

$$K_2 = \frac{F_A^{(2)} F_{C_2}^{(3)} e^{-\lambda \tau_{\mathrm{CTGF}}}}{(\lambda - F_A^{(3)})(\lambda - F_D^{(2)}) - F_A^{(2)} F_D^{(3)}} \tag{21}$$

and each $F^{(i)}$ is evaluated at its appropriate steady state. Finally, define the TGF gain as:

$$\gamma_{\mathrm{TGF}} = \frac{\bar{C_1}'(L_{\mathrm{TGF}}) F_D^{(0)}(\bar{D}) F_A^{(2)}(\bar{D}, \bar{A}) F_{C_1}^{(3)}(\bar{D}, \bar{A}, \bar{C_1}, \bar{C_2})}{F^{(0)}(\bar{D})} \tag{22}$$

and the CTGF gain as:

$$\gamma_{\mathrm{CTGF}} = \frac{\bar{C_2}'(L_{\mathrm{DT}}) F_D^{(a)}(\bar{D}, L_{\mathrm{DT}}) F_A^{(2)}(\bar{D}, \bar{A}) F_{C_2}^{(3)}(\bar{D}, \bar{A}, \bar{C_1}, \bar{C_2})}{F^{(a)}(\bar{D}, L_{\mathrm{DT}})} \tag{23}$$

In Eq. 22, the product $F_D^{(0)} F_A^{(2)} F_{C_1}^{(3)}$ describes the response of the flow $F^{(0)}$ at L_{TGF} to a perturbation in the concentration at the MD. Analogously, in Eq. 23, the product $F_D^{(a)} F_A^{(2)} F_{C_2}^{(3)}$ describes the response of the flow $F^{(a)}$ at L_{CTGF} to a perturbation in the concentration at the distal tubule outflow. We also assume that the fluid is incompressible and thus an increase (or decrease) in flow $F^{(0)}$ or $F^{(a)}$ will result in an instantaneous translation of the concentration profile. Therefore, the terms $\bar{C_1}'(L_{\mathrm{TGF}})$ and $\bar{C_2}'(L_{\mathrm{DT}})$ describe the instantaneous change in concentration after a small perturbation in flow. The terms $F^{(0)}(\bar{D}, L_{\mathrm{TGF}})$ and $F^{(a)}(\bar{D}, L_{\mathrm{CTGF}})$ in the denominators are nondimensionalizing constants. Taken altogether, we have defined the TGF and CTGF gains. The gain for TGF will take positive values, while CTGF gain will take negative values. For both, larger values in absolute value correspond to greater sensitivity.

We attempt to substitute both γ_{TGF} and γ_{CTGF} into the characteristic equation (Eq. 19). Notationally, let INT_1 be the integral in the first term of

Eq. 19, and INT_2 be the second integral. Explicitly

$$\mathrm{INT}_1 = \int_0^{L_{\mathrm{TGF}}} \bar{C_1}(z) e^{\lambda(L_{\mathrm{TGF}}-z)/F^{(0)}(\bar{D})} \exp\Bigg(-\int_z^{L_{\mathrm{TGF}}} \left(\frac{F_{C_1}^{(1)}(\bar{C_1}(y))}{F^{(0)}(\bar{D})} \right) dy \Bigg) dz \tag{24}$$

$$\mathrm{INT}_2 = \int_0^{L_{\mathrm{DT}}} \left(\frac{\frac{\partial}{\partial z}(F_D^{(a)}(\bar{D}, z)\bar{C_2}(z))}{F^{(a)}(\bar{D}, z)} \right) \exp\Bigg(\int_z^{L_{\mathrm{DT}}} \left(\frac{\lambda - \frac{\partial}{\partial y}F^{(a)}(\bar{D}, y) - F_{C_2}^{(b)}(\bar{C_2}(y))}{F^{(a)}(\bar{D}, y)} \right) dy \Bigg) dz \tag{25}$$

and denote

$$K_{denom} = (\lambda - F_A^{(3)})(\lambda - F_D^{(2)}) - F_A^{(2)} F_D^{(3)} \tag{26}$$

With these notations, we rewrite the characteristic equation (Eq. 19) to incorporate γ_{TGF} and γ_{CTGF}.

$$\begin{aligned} 1 = &-\frac{\gamma_{\mathrm{TGF}} e^{-\lambda\tau_{\mathrm{TGF}}}}{K_{denom}\bar{C_1}'(L_{\mathrm{TGF}})}(\mathrm{INT}_1) - \frac{\gamma_{\mathrm{CTGF}} e^{-\lambda\tau_{\mathrm{CTGF}}}}{K_{denom}\bar{C_2}'(L_{\mathrm{DT}})} \left(\frac{F_D^{(0)}(\bar{D})}{F^{(0)}(\bar{D})} \right) \left(\frac{F^{(a)}(\bar{D}, L_{\mathrm{DT}})}{F_D^{(a)}(\bar{D}, L_{\mathrm{DT}})} \right) (\mathrm{INT}_1) \\ &- \frac{\gamma_{\mathrm{CTGF}} e^{-\lambda\tau_{\mathrm{CTGF}}}}{K_{denom}\bar{C_2}'(L_{\mathrm{DT}})} \left(\frac{F^{(a)}(\bar{D}, L_{\mathrm{DT}})}{F_D^{(a)}(\bar{D}, L_{\mathrm{DT}})} \right) (\mathrm{INT}_2) \end{aligned} \tag{27}$$

Given a set of parameters, we can solve for $\lambda_1, \lambda_2, \lambda_3, ... \in \mathbb{C}$ that satisfy Eq. 27 (note that there are an infinite number of solutions in $\mathbb{C}$ because of the exponential terms), and this enabled us to predict model behavior. Parameter regimes where $\mathrm{Re}(\lambda_n) < 0$ imply that a time-independent steady state is obtained, while regimes where $\mathrm{Re}(\lambda_n) > 0$ imply limit cycle oscillations. Hence, given two parameters to analyze (e.g. τ_{CTGF} and γ_{CTGF}), we can plot a curve on the 2D parameter space where the pair of parameters result in $\mathrm{Re}(\lambda_n) = 0$. This curve is a Hopf bifurcation curve, partitioning the parameter space into regions where there are limit cycles from those regions where there are steady state solutions.

Solving for λ_n was done by gradient descent; derivatives appearing in the characteristic equation were computed by midpoint approximation, and integrals were computed using trapezoidal rule.

3.2. Bifurcation results

Figure 3 shows the bifurcation diagram for τ_{TGF}, the TGF delay, versus γ_{CTGF}, the positive feedback gain. We observe that for a given τ_{TGF}, the

strength of positive feedback must be sufficiently weak (γ_{CTGF} less negative) in order to observe limit cycles. When the positive feedback is too strong, limit cycles are overwhelmed and we obtain a steady state. Like the results previously observed in Ford Versypt et al. (2015), τ_{TGF} must be made sufficiently large in order to observe limit cycles.

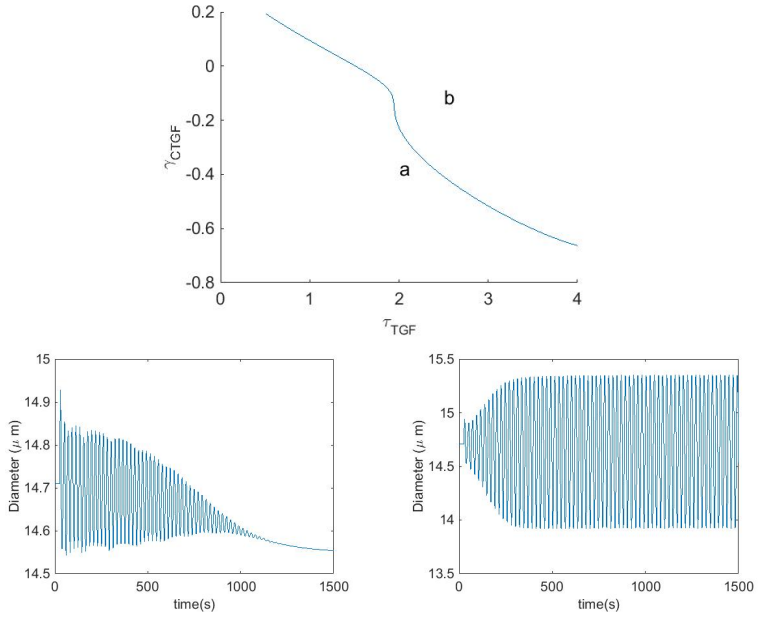

(a) (b)

Figure 3: Bifurcation diagrams and corresponding numerical simulations for τ_{TGF} vs. γ_{CTGF}. Panel (a), simulation results showing afferent arteriole diameter approaching a time-independent steady state following a transient perturbation, obtained for $(\tau_{\mathrm{TGF}}, \gamma_{\mathrm{CTGF}}) = (2.0, -0.3827)$. Panel (b), analogous results showing a limit cycle oscillation, obtained for $(\tau_{\mathrm{TGF}}, \gamma_{\mathrm{CTGF}}) = (2.5, -0.1094)$.

Figure 4 shows the bifurcation diagram for τ_{CTGF}, the CTGF delay, versus γ_{CTGF}. As observed above, the strength of positive feedback must be sufficiently weak in order to observe limit cycle activity. However, it is interesting that τ_{CTGF}, the delay of the positive feedback signal, appears to not affect the qualitative behavior of the system, at least when compared with the positive feedback gain.

We also examined the bifurcation diagram corresponding to τ_{TGF}, the time delay for TGF, versus γ_{TGF}, the negative feedback gain (Fig. 5). We see that to obtain limit cycle behavior, γ_{TGF} must be sufficiently large. Fur-

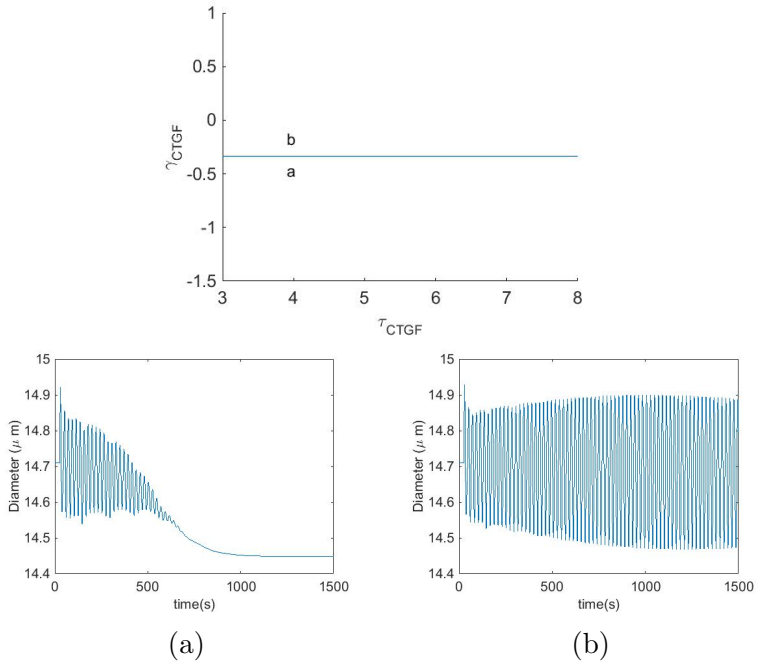

Figure 4: Bifurcation results for τ_{CTGF} versus γ_{CTGF}. Panel (a), simulations results showing afferent arteriole diameter approaching a time-independent steady state following a transient perturbation, obtained for $(\tau_{\mathrm{CTGF}}, \gamma_{\mathrm{CTGF}}) = (4.0, -0.4922)$. Panel (b), analogous results showing a limit-cycle oscillation, obtained for $(\tau_{\mathrm{CTGF}}, \gamma_{\mathrm{CTGF}}) = (4.0, -0.2734)$.

thermore, for this diagram, we plotted many solutions to our characteristic equation (Eq. 27), so we have partitioned the parameter space into regions where different frequencies of oscillation occur. In particular, in our model with positive feedback, we were able to obtain limit cycle oscillations of the first harmonic dominant frequency (Fig. 5c), consistent with observations in prior work on TGF alone (Ford Versypt et al., 2015).

Finally, Figure 6a shows the bifurcation diagram for τ_{TGF} versus τ_a, the time constant for afferent arteriole activation response, and Figure 6b shows the bifurcation diagram for τ_{TGF} versus τ_d, the time constant for afferent arteriole diameter response. As before, we see that one way to produce limit cycles is to have τ_{TGF} large. However, these plots suggest that limit cycles also occur when τ_a or τ_d is increases.

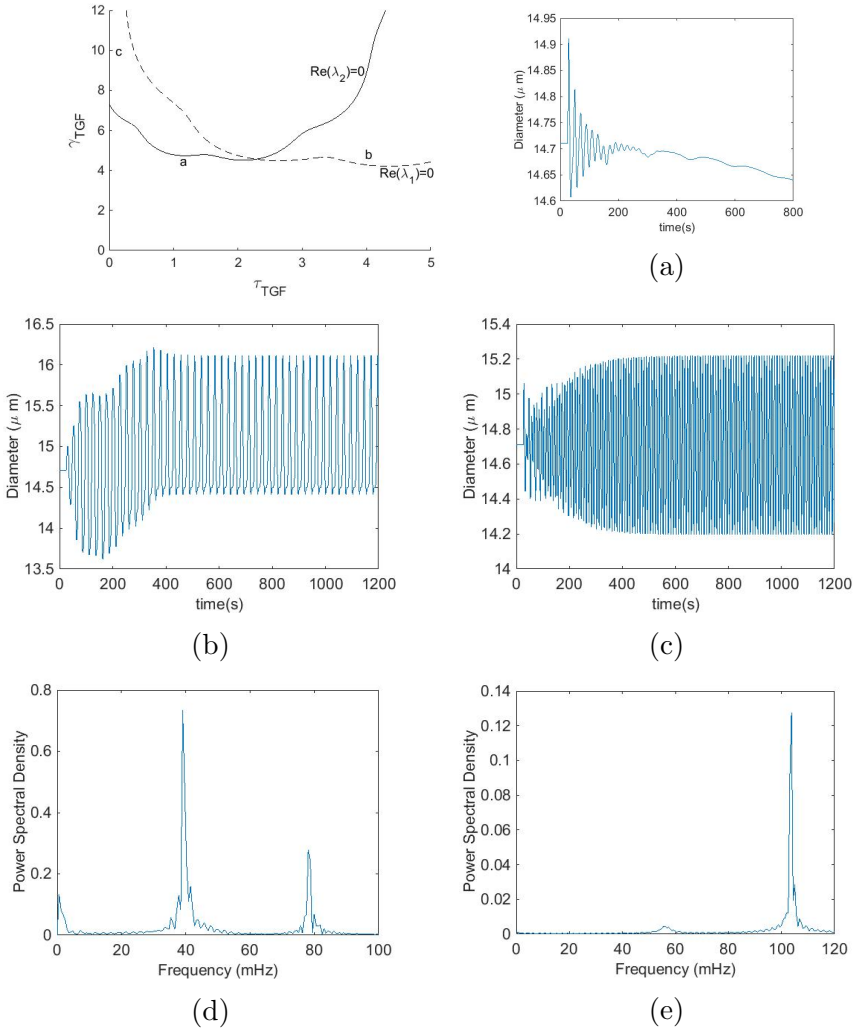

Figure 5: Bifurcation diagram for τ_{TGF} versus γ_{TGF} and corresponding numerical simulations. Power spectra corresponding to (b) and (c) are shown in (d) and (e), respectively

3.3. Slow Oscillations

As previously noted, modeling studies on TGF have demonstrated that some parameter regimes may yield sustained oscillations at a frequency of 30-40mHz in SNGFR, chloride concentration, diameter of the afferent arteriole, and other related variables. Using our expanded model that incorporates CTGF, we seek to identify model parameters that give rise to oscillations having the slower ($\sim$ 10 mHz) frequency observed in experimental records

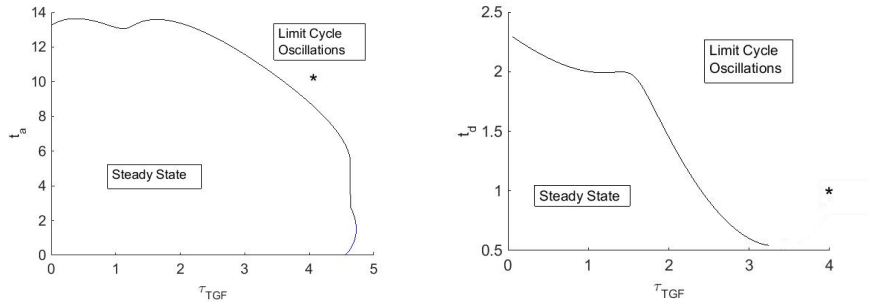

(a) (b)

Figure 6: Panel (a), bifurcation diagram for τ_{TGF} versus t_a. Panel (b), bifurcation diagram for τ_{TGF} versus t_d. * indicates base-case parameter values.

(Fig. 2) but could not be explained by TGF alone.

Figure 7 shows the afferent arteriole diameter, Cl^- concentration at MD, and Cl^- concentration at the distal tubule outflow as functions of time. Two different parameter sets were used, one generating sustained limit cycle behavior (panels (a) and (c)) and the other reaching an eventual steady-state (panels (b) and (d)). In both cases however, a slower oscillation at a frequency of around 10mHz can be observed in the first $\sim$800s before disappearing. Note that for other parameter sets the slow mode may not be present at all (see e.g. simulations in Figures 3–5).

To investigate the transient nature of the slow oscillation, we examine the behavior of $[Cl^-]$ at the distal tubule outflow. As can be seen in Figure 7, so long as Cl^- concentration at the distal tubule outflow hovers around its operating point, the system's oscillations include a slow mode. However, because the distal tubule feedback is a positive one, once $[Cl^-]$ deviates sufficiently far from its operating point, it diverges. As a result, the distal tubule feedback signal becomes sustained, not oscillatory, and the slow oscillations disappear.

4. Discussion

In this project, we expanded previous models of the kidney's TGF mechanism (Arciero et al., 2015; Ford Versypt et al., 2015) to include positive feedback from the connecting tubule (CTGF) in hopes of obtaining more physiologically realistic behaviors. Using both a bifurcation analysis and numerical simulations, we attempted to understand the interaction between

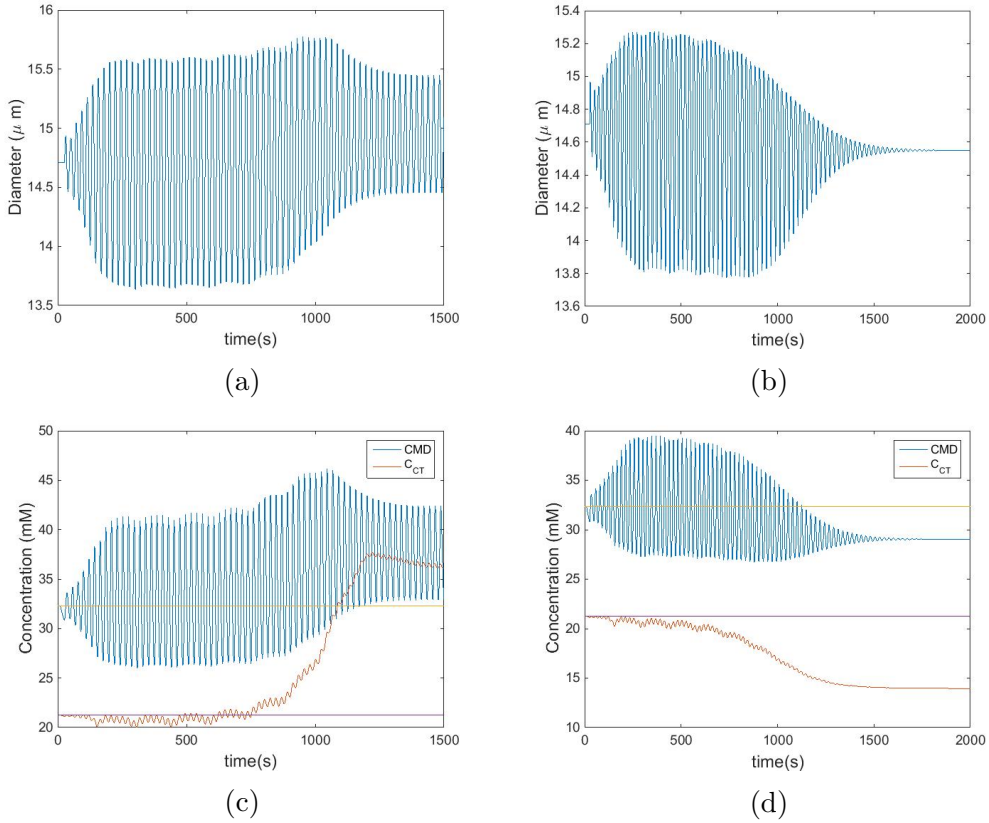

Figure 7: Two simulations showing the imprint of a slow oscillation. Panels (a) and (b), afferent arteriole diameter as a function of time; panels (c) and (d), corresponding $[Cl^-]$ at the macula densa (blue curves) and at the distal tubule outlet (red curves). In one case (left column), a limit-cycle oscillation is predicted; in the other case (right column), the solution converges to a time-independent steady state. In both cases, the slow mode appears to be transient. Horizontal lines in panels (c) and (d) denote TGF and CTGF $[Cl^-]$ operating points. Parameters: in (a) and (c) we set $\tau_{\rm TGF} = 2$, $\tau_{\rm CTGF} = 8$, $\tau_d = 2.4$, $\tau_a = 10$; in (b) and (d) we set $\tau_{\rm TGF} = 3.5$, $\tau_{\rm CTGF} = 8$, $\tau_d = 2$, $\tau_a = 3.5$.

TGF and CTGF. Our bifurcation analysis revealed that even in the presence of positive feedback, we were still able to produce limit cycle behaviors over a wide range of parameter regimes. Furthermore, we found that the model can generate distinct dominant frequencies: we were able to isolate both the frequency that is physiologically observed between and 25-40 mHz as well as its harmonic frequency between 100 and 120mHz. Numerical simulations were able to confirm this variety of behaviors predicted by our bifurcation analy-

sis (Fig. 5). In addition, model results suggest that the presence of CTGF lowers the stability of the system at small TGF delay values (i.e. oscillatory solutions are found at lower TGF gain values) but increases its stability at larger TGF delays (Fig. 8).

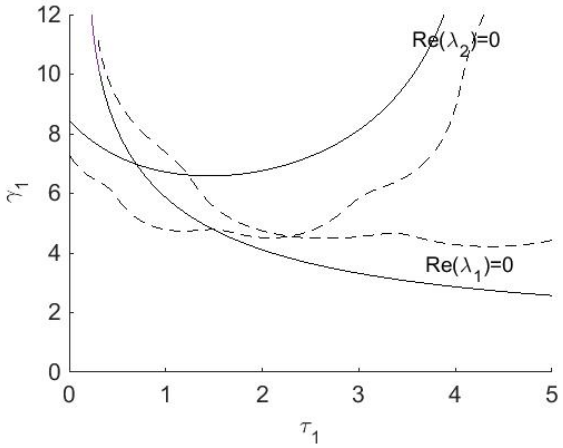

Figure 8: Bifurcation diagram in the τ_{TGF}–γ_{TGF} plane, obtained with CTGF (dashed lines) and without CTGF (solid lines).

TGF alone is able to beget limit cycle oscillations under certain parameter regimes with a dominant frequency of 25-40mHz. Physiologically however, one can observe an additional slower frequency. According to our new model, CTGF is one potential cause of this. We hypothesized that CTGF can be viewed as periodic perturbations on the TGF system, and due to the longer CTGF transit time compared to TGF, the resulting CTGF-induced oscillations should exhibit a lower frequency. Figure 7 shows that under certain parameter regimes, the TGF-CTGF interactions can indeed produce an underlying slow frequency. However, in comparing Figures 2 and 7, we see that the slow oscillation is weaker compared to experimental records and is transient.

Figure 7 (c) and (d) provide an explanation as to why the slow oscillation is transient. The slow oscillation is present when [Cl^-] at the distal tubule outflow oscillates close to its operating point, so the positive feedback signals sent act as periodic perturbations of TGF. In our plots (Fig. 7), this pattern is maintained for the first ∼800ms. However, this oscillation is unstable, as positive feedback eventually drives [Cl^-] at the distal tubule outflow far from its operating point. When the deviation is large, the CTGF signal

becomes sustained rather than oscillatory, resulting in the disappearance of the CTGF-mediated slow oscillation.

However, such a large deviation of distal [Cl^-] from its operating point as seen in Fig. 7(c) and (d) may not be physically realistic due to an implicit feedback mechanism underlying tubular water reabsorption. Recall that unlike the TAL, the distal tubule is water permeable. Thus, when fluid osmolality in the distal tubule becomes high, water flows into the tubule, lowering Cl^- concentration; and when osmolality decreases, water flows out of the tubule, raising Cl^- concentration. In other words, water transport should depend on tubular fluid [Cl^-] in a way that keeps [Cl^-] close to its operating point. However, this is not modeled by our equations because the model represents only Cl^-, whereas tubular water transport depends on many other solutes such as Na^+, K^+, urea, etc. We hypothesize that more realistic model taking into account this osmolality control may in fact generate a sustained slow oscillation. Regardless, because biological systems are invariably under external perturbations— specificaly in this case, blood pressure is constantly perturbed by breathing, heart beats, etc.— even a transient slow oscillation may persist long enough to be observed in experimental records.

Despite its limitations, the current model has revealed, *for the first time*, the potential of CTGF as the mediator, or one of the mediators, of the slow oscillation in tubular flow variables, and its role may be revisited using a more comprehensive model.

Acknowledgements

I would like to sincerely thank Dr. Anita Layton for her mentorship in this project. This research was supported by the Mathematics Department at Duke University, PRUV undergraduate research program.

Appendix A. Derivation of Characteristic Equation

We linearize Eqs. 14–17 about the steady state $(\bar{C}_1, \bar{C}_2, \bar{D}, \bar{A})$ and drop the steady-state terms to obtain

$$\frac{\partial}{\partial t}\begin{pmatrix} C_1(x,t) \\ C_2(x,t) \\ D(t) \\ A(t) \end{pmatrix} = \begin{pmatrix} F^{(0)}(\bar{D})\frac{\partial}{\partial x} + F^{(1)}_{C_1}(\bar{C}_1(x)) & 0 & F^{(0)}_D(\bar{D})\frac{\partial}{\partial x}\bar{C}_1(x) & 0 \\ 0 & \frac{\partial}{\partial x}F^{(a)}(\bar{D},x) + F^{(a)}(\bar{D},x)\frac{\partial}{\partial x} + F^{(b)}_{C_2}(\bar{C}_2(x)) & \frac{\partial}{\partial x}F^{(a)}_D(\bar{D},x)\bar{C}_2(x) + F^{(a)}_D(\bar{D},x)\frac{\partial}{\partial x}\bar{C}_2(x) & 0 \\ 0 & 0 & F^{(2)}_D(\bar{D},\bar{A}) & F^{(2)}_A(\bar{D},\bar{A}) \\ F^{(3)}_{C_1}(\bar{D},\bar{A},\bar{C}_1(L_{\mathrm{TGF}}),\bar{C}_2(L_{\mathrm{DT}}))\mathcal{L}_1 & F^{(3)}_{C_2}(\bar{D},\bar{A},\bar{C}_1(L_{\mathrm{TGF}}),\bar{C}_2(L_{\mathrm{DT}}))\mathcal{L}_2 & F^{(3)}_D(\bar{D},\bar{A},\bar{C}_1(L_{\mathrm{TGF}}),\bar{C}_2(L_{\mathrm{DT}})) & F^{(3)}_A(\bar{D},\bar{A},\bar{C}_1(L_{\mathrm{TGF}}),\bar{C}_2(L_{\mathrm{DT}})) \end{pmatrix}\begin{pmatrix} C_1(x,t) \\ C_2(x,t) \\ D(t) \\ A(t) \end{pmatrix} \tag{A.1}$$

where $\mathcal{L}_1 C_1(x,t) := C_1(L_{\mathrm{TGF}}, t-\tau_{\mathrm{TGF}})$ and $\mathcal{L}_2 C_2(x,t) := C_2(L_{\mathrm{DT}}, t-\tau_{\mathrm{CTGF}})$. We then substitute into Eq. A.1 the solution given in Eq. 18 to obtain

$$\lambda\begin{pmatrix} f_1(x) \\ f_2(x) \\ b_1 \\ b_2 \end{pmatrix} = \begin{pmatrix} F^{(0)}(\bar{D})f_1'(x) + F^{(1)}_{C_1}(\bar{C}_1(x))f_1(x) + F^{(0)}_D(\bar{D})\frac{\partial}{\partial x}\bar{C}_1(x)b_1 \\ \frac{\partial}{\partial x}F^{(a)}(\bar{D},x)f_2(x) + F^{(a)}(\bar{D},x)f_2'(x) + F^{(b)}_{C_2}(\bar{C}_2(x))f_2(x) + \frac{\partial}{\partial x}F^{(a)}_D(\bar{D},x)\bar{C}_2(x)b_1 + F^{(a)}_D(\bar{D},x)\frac{\partial}{\partial x}\bar{C}_2(x)b_1 \\ F^{(2)}_D(\bar{D},\bar{A})b_1 + F^{(2)}_A(\bar{D},\bar{A})b_2 \\ F^{(3)}_{C_1}(\bar{D},\bar{A},\bar{C}_1(L_{\mathrm{TGF}}),\bar{C}_2(L_{\mathrm{DT}}))f_1(L_{\mathrm{TGF}})e^{-\lambda\tau_{\mathrm{TGF}}} + F^{(3)}_{C_2}(\bar{D},\bar{A},\bar{C}_1(L_{\mathrm{TGF}}),\bar{C}_2(L_{\mathrm{DT}}))f_2(L_{\mathrm{DT}})e^{-\lambda\tau_{\mathrm{CTGF}}}\ldots \\ +F^{(3)}_D(\bar{D},\bar{A},\bar{C}_1(L_{\mathrm{TGF}}),\bar{C}_2(L_{\mathrm{DT}}))b_1 + F^{(3)}_A(\bar{D},\bar{A},\bar{C}_1(L_{\mathrm{TGF}}),\bar{C}_2(L_{\mathrm{DT}}))b_2 \end{pmatrix} \tag{A.2}$$

From the last row, we solve for b_2:

$$b_2 = \frac{F^{(3)}_{C_1} f_1(L_{\mathrm{TGF}})e^{-\lambda\tau_{\mathrm{TGF}}} + F^{(3)}_{C_2} f_2(L_{\mathrm{DT}})e^{-\lambda\tau_{\mathrm{CTGF}}} + F^{(3)}_D b_1}{\lambda - F^{(3)}_A} \tag{A.3}$$

and substituting this into the equation given by the third row, we obtain an expression for b_1

$$b_1 = \frac{F^{(2)}_A F^{(3)}_{C_1} f_1(L_{\mathrm{TGF}})e^{-\lambda\tau_{\mathrm{TGF}}} + F^{(2)}_A F^{(3)}_{C_2} f_2(L_{\mathrm{DT}})e^{-\lambda\tau_{\mathrm{CTGF}}}}{(\lambda - F^{(3)}_A)(\lambda - F^{(2)}_D - F^{(2)}_A F^{(3)}_D)} \tag{A.4}$$

From the first row, we have the following differential equation:

$$f_1'(x) = \left(\frac{\lambda - F^{(1)}_{C_1}(\bar{C}_1(x))}{F^{(0)}(\bar{D})}\right) f_1(x) - \left(\frac{F^{(0)}_D(\bar{D})\bar{C}_1'(x)}{F^{(0)}(\bar{D})}\right) b_1 \tag{A.5}$$

And from the second row, the following differential equation results:

$$f_2'(x) = \left(\frac{\lambda - \frac{\partial}{\partial x}F^{(a)}(\bar{D},x) - F_{C_2}^{(b)}(\bar{C}_2(x))}{F^{(a)}(\bar{D},x)}\right)f_2(x) - \left(\frac{\frac{\partial}{\partial x}(F_D^{(a)}(\bar{D},x)\bar{C}_2(x))}{F^{(a)}(\bar{D},x)}\right)b_1 \quad \text{(A.6)}$$

Solving the ODE for f_1, we obtain

$$f_1(x) = -\left(\frac{F_D^{(0)}(\bar{D})}{F^{(0)}(\bar{D})}\right)b_1 \exp\left(\int_0^x \left(\frac{\lambda - F_{C_1}^{(1)}(\bar{C}_1(y))}{F^{(0)}(\bar{D})}\right)dy\right)\times$$
$$\int_0^x \bar{C_1}'(z)\exp\left(-\int_0^z \left(\frac{\lambda - F_{C_1}^{(1)}(\bar{C}_1(y))}{F^{(0)}(\bar{D})}\right)dy\right)dz \quad \text{(A.7)}$$

Evaluating at $x = L_{\text{TGF}}$, we obtain

$$f_1(L_{\text{TGF}}) = -\left(\frac{F_D^{(0)}(\bar{D})}{F^{(0)}(\bar{D})}\right)b_1 \int_0^{L_{\text{TGF}}} \bar{C_1}'(z)e^{\lambda(L_{\text{TGF}}-z)/F^{(0)}(\bar{D})} \exp\left(-\int_z^{L_{\text{TGF}}} \left(\frac{F_{C_1}^{(1)}(\bar{C}_1(y))}{F^{(0)}(\bar{D})}\right)dy\right)dz \quad \text{(A.8)}$$

Recall that our initial condition enforces $f_2(0) = f_1(L_{\text{TGF}})$. Thus, the ODE for f_2 gives

$$f_2(x) = -b_1 \exp\left(\int_0^x \left(\frac{\lambda - \frac{\partial}{\partial y}F^{(a)}(\bar{D},y) - F_{C_2}^{(b)}(\bar{C}_2(y))}{F^{(a)}(\bar{D},y)}\right)dy\right)\int_0^x \left(\frac{\frac{\partial}{\partial z}(F_D^{(a)}(\bar{D},z)\bar{C}_2(z))}{F^{(a)}(\bar{D},z)}\right)\times$$
$$\exp\left(-\int_0^z \left(\frac{\lambda - \frac{\partial}{\partial y}F^{(a)}(\bar{D},y) - F_{C_2}^{(b)}(\bar{C}_2(y))}{F^{(a)}(\bar{D},y)}\right)dy\right)dz + f_1(L_{\text{TGF}}) \quad \text{(A.9)}$$

Evaluating this at $x = L_{\text{DT}}$, we get

$$f_2(L_{\text{DT}}) = -b_1 \int_0^{L_{\text{DT}}} \left(\frac{\frac{\partial}{\partial z}(F_D^{(a)}(\bar{D},z)\bar{C}_2(z))}{F^{(a)}(\bar{D},z)}\right)\times$$
$$\exp\left(\int_z^{L_{\text{DT}}} \left(\frac{\lambda - \frac{\partial}{\partial y}F^{(a)}(\bar{D},y) - F_{C_2}^{(b)}(\bar{C}_2(y))}{F^{(a)}(\bar{D},y)}\right)dy\right)dz + f_1(L_{\text{TGF}}) \quad \text{(A.10)}$$

We combine the expressions for $f_2(L_{\text{DT}})$, $f_1(L_{\text{TGF}})$, and b_1 to obtain the characteristic equation (Eq. 19).

References

Arciero, J., Ellwein, L., Ford Versypt, A., Makrides, E., Layton, A., 2015. Modeling blood flow control in the kidney. In: Applications of Dynamical Systems in Biology and Medicine. Springer, pp. 55–73.

Eaton, D. C., Pooler, J. P., 2013. Vander's Renal Physiology, 8th Edition. McGrawHill Medical, New York.

Ford Versypt, A., Makrides, E., Arciero, J., Ellwein, L., Layton, A., 2015. Bifurcation study of blood flow control in the kidney. Mathematical biosciences 263, 169–179.

Holstein-Rathlou, N., Leyssac, P., 1986. TGF-mediated oscillations in the proximal intratubular pressure: Differences between spontaneously hypertensive rats and Wistar-Kyoto rats. Acta Physiol Scand 126, 333–339.

Layton, A., Edwards, A., 2014. Mathematical Modeling of Renal Physiology (Lecture Notes on Mathematical Modelling in the Life Sciences). Springer.

Pennell, J., Lacy, F., Jamison, R., 1974. An in vivo study of the concentrating process in the descending limb of Henle's loop. Kidney Int 5, 337–347.

Ren, Y., D'Ambrosio, M., Liu, R., Ragano, P., Garvin, J., 2010. Enhanced myogenic response in the afferent arteriole of spontaneously hypertensive rats. Am J Physiol Heart Circ Physiol 298, H1769–H1775.

Ren, Y., Garvin, J., Liu, R., Carretero, O., 2007. Crosstalk between the connecting tubule and the afferent arteriole regulates renal microcirculation. Kidney Int 71, 1116–1121.

Table 1: Glossary. AA, afferent arteriole. CTGF, connecting tubule glomerular feedback. DT, distal convoluted tubular. MD, macula densa. TAL, thick ascending limb. TGF, tubuloglomerular feedback. VSM, vascular smooth muscle.

Symbol	Description	Units	Value
α	Fraction of arteriolar flow entering TAL	-	0.0168
C_0	Tubular fluid [Cl^-] at TAL entrance	mM	275
c_2	VSM TGF sensitivity	cm/dyn	1.80
c_3	VSM CTGF sensitivity	cm/dyn	1.40
c_{act}	VSM peak tension	dyn/cm	274.19
$c_{act,1}$	VSM length dependence	-	0.75
$c_{act,2}$	VSM tension range	-	0.38
c_{CTGF}	VSM [Cl^-] sensitivity in distal tubule	cm/dyn	3×10^5
c_{TGF}	VSM [Cl^-] sensitivity in TAL	cm/dyn	3×10^5
$C_{\mathrm{CTGF,op}}$	CTGF operating [Cl^-]	mM	21.24
$C_{\mathrm{TGF,op}}$	TGF operating [Cl^-]	mM	32.32
$C_{e,\mathrm{MD}}$	Interstitial [Cl^-] at MD	mM	150
c_{myo}	VSM tension sensitivity	cm/dyn	0.159
c_{pass}	Passive tension strength	dyn/cm	220
$c_{pass,1}$	Passive tension sensitivity	-	11.47
c_{tone}	VSM constant	-	13.29
D_0	Passive AA diameter	μm	33
J	Fraction of water reabsorbed along DT	-	0.835
$K_{m,DT}$	Michaelis-Menten constant for DT	mM	40.0
$K_{m,TAL}$	Michaelis-Menten constant for TAL	mM	70.0
l	Length of AA	cm	0.031
L_{CTGF}	Combined length of TAL & distal tubule	cm	2.5
L_{DT}	Length of distal tubule	cm	2
L_{TGF}	Length of TAL	cm	0.5
p	TAL Cl^- permeability	cm/s	1.5×10^{-5}
P	Tubular fluid pressure at TAL entrance	mmHg	100
ΔP	Pressure drop	mmHg	50
P_{avg}	Midpoint pressure in AA, specified	mmHg	75
$P_{avg,c}$	Midpoint pressure in AA, control state	mmHg	75
Q_A	AA blood flow rate	nl/min	355.4
r	TAL luminal radius	cm	1.0×10^{-3}
τ_{CTGF}	Time delay, connecting tubule to AA response	s	8
τ_{TGF}	Time delay, MD to AA response	s	4
t_a	Time constant for AA activation response	s	10
t_d	Time constant for AA diameter response	s	1
μ	Blood viscosity	cP	4.14
$V_{max,DT}$	Maximum active transport rate in DT	mol/(cm^2·s)	55×10^{-8}
$V_{max,TAL}$	Maximum active transport rate in TAL	mol/(cm^2·s)	14.5×10^{-9}